Near-Field Thermophotonic Systems for Low-Grade Waste-Heat Recovery
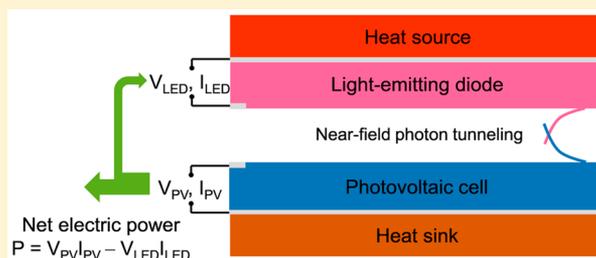
Bo Zhao,[†] Parthiban Santhanam,[†] Kaifeng Chen,[†,‡] Siddharth Buddhiraju,[†] and Shanhui Fan[*,†]

[†]Department of Electrical Engineering and [‡]Department of Applied Physics, Ginzton Laboratory, Stanford University, Stanford, California 94305, United States

ABSTRACT: Low-grade waste heat contains an enormous amount of exergy that can be recovered for renewable-energy generation. Current solid-state techniques for recovering low-grade waste heat, such as thermoelectric generators and thermophotovoltaics, however, are limited by low conversion efficiencies or power densities. In this work, we propose a solid-state near-field thermophotonic system. The system consists of a light-emitting diode (LED) on the hot side and a photovoltaic (PV) cell on the cold side. Part of the generated power by the PV cell is used to positively bias the LED. When operating in the near-field regime, the system can have power density and conversion efficiency significantly exceeding the performance of current solid-state approaches for low-grade waste-heat recovery. For example, when the gap spacing is 10 nm and the hot side and cold side are, respectively, 600 and 300 K, we show that the generated electric power density and thermal-to-electrical conversion efficiency can reach 9.6 W/cm^2 and 9.8%, respectively, significantly outperforming the current record-setting thermoelectric generators. We identify the alignment of the band gaps of the LED and the PV cell, the appropriate choice of thickness of the LED and PV cell to mitigate the effect of non-radiative recombination, and the use of highly reflective back mirrors as key factors that affect the performance of the system. Our work points to the significant potential of photonic systems for the recovery of low-grade waste heat.

KEYWORDS: Near-field thermophotonics, photon chemical potential, waste-heat recovery, photon tunneling

More than half of the energy that the infrastructure handles globally is rejected to the environment as waste heat eventually. The waste heat in the United States alone can potentially produce over 15 GW of electricity.[1] Based on its source temperature, waste heat can be roughly categorized as high-grade (>900 K), medium-grade (~500−900 K), and low-grade (<500 K).[2] Research on power generation from waste heat has been largely focused on the medium- to high-grade types because low-grade waste heat is difficult to be efficiently recovered to electricity using current technologies.[2] However, the low-grade waste heat sources in total contain more amount of exergy (the maximum amount of energy one can possibly recover) compared with the waste heat sources at higher temperatures.[2] Therefore, recovering low-grade waste heat has great economic and environmental impact.

Thermoelectric generators are among the most commonly used solid-state techniques for recovering waste heat from sources at low and medium temperatures. Tremendous progress has been made toward developing high figure-of-merit (ZT) thermoelectric generators.[3,4] Recently, a thermoelectric generator demonstrated a record-high power density of about 5 W/cm^2, operating between a heat source at around 600 K and a heat sink at 300 K, although the efficiency (~5%) was relatively low (ZT ≈ 0.6).[5]

Photonic approaches such as thermophotovoltaics represent an emerging solid-state approach for waste heat recovery. Compared to the thermoelectric approach, the photonic approach can provide higher conversion efficiencies,[6−8] but the power densities are much lower because thermal radiation typically carries far less power density compared to heat conduction. This remains true even in the near-field regime, in which radiative heat transfer is significantly enhanced as compared to the far field.[9−13] For example, for a source temperature of 600 K and a gap spacing of 10 nm, a recent simulation of a near-field thermophotovoltaics system, which consists of a thermal emitter based on indium tin oxide and an InAs photovoltaic cell, yields an efficiency of 15%, which is higher than the thermoelectric approach but with a power density of approximately 0.5 W/cm^2 that is significantly lower than the thermoelectric approach.[11] The fundamental challenge in the photonics approach for waste heat recovery, therefore, lies in further enhancement of power density while maintaining high efficiency.

In this Letter, we propose a near-field thermophotonic system for high-performance, low-grade waste heat recovery. Compared to a standard thermophotovoltaic system, a thermophotonic system replaces the passive thermal emitter at the hot side with a light-emitting diode (LED). The LED is driven by part of the electric power generated by the photovoltaic cell. The LED can
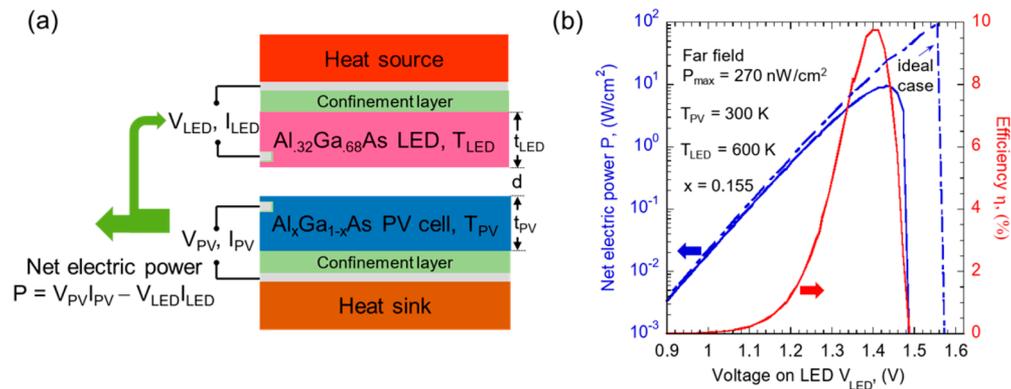
(a)

(b)

Figure 1. (a) Schematic of the proposed system. The emitter is an $Al_{.32}Ga_{.68}As$ LED, and the PV cell is $Al_{.155}Ga_{.845}As$. The temperatures of the PV cell and the LED are T_{PV} and T_{LED}, respectively. The thicknesses of the cell and the LED are t_{PV} and t_{LED}, respectively, and the gap spacing between the LED and the PV cell is denoted by d. The forward biases on the cell and LED are V_{PV} and V_{LED}, respectively, while the current densities are I_{PV} and I_{LED}, respectively. Both the LED and cell have Ag back mirrors (thick silvery lines) for photon recycling and serves as one metal contact. The active regions of the LED and PV cell are separated from the metal contacts by $Al_{.8}Ga_{.2}As$ carrier confinement layers. We assume the confinement layers in contact with the Ag mirrors are both 500 nm thick. (b) The net power and conversion efficiency of the proposed system as a function of the bias on the LED, with the LED temperature set to 600 K. The curves are computed with $d = 10$ nm. The power and efficiency curves are calculated with all the realistic nonidealities of the system. t_{PV} and t_{LED} are set to be 900 nm. In obtaining the power curve for the ideal case, we assume the LED and the PV cell are infinitely thick, the photons are perfectly recycled, and the non-radiative recombination rate is 0.

boost the radiative transfer and, thus, can potentially yield higher power densities compared to using a passive thermal emitter. This thermophotonic approach, initially proposed by Harder and Green[14] for solar energy harvesting, has been recently considered for electroluminescent cooling.[15−17] However, the potential of thermophotonics for waste-heat recovery has not been discussed. Here, we show that the thermophotonic approach, when operating in the near-field regime, can result in the recovery of low-grade waste heat with both the power density and the efficiency significantly exceeding current solid-state approaches.

As a specific example (Figure 1), we consider the case in which the hot and cold sides are maintained at temperatures of 600 and 300 K, respectively. The hot side of the system consists of an LED made of $Al_{.32}Ga_{.68}As$. This material has been commercially used to make high-efficiency red LEDs.[18] The cold side of the system consists of a photovoltaic (PV) cell made of $Al_{.155}Ga_{.845}As$. The thicknesses of both the PV cell and the LED are assumed to be 900 nm. We assume 500 nm wide band gap transparent $Al_{.8}Ga_{.2}As$ confinement layers at the back sides of the active regions of the PV cell and LED.[18] We use Ag mirrors at the back sides of the confinement layers for photon-recycling purposes. In this system, the emission of the LED is injected into the photovoltaic cell, and part of the electric power generated on the photovoltaic cell is then fed back to drive the LED. Our numerical results show that in the near-field regime when the LED and the photovoltaic cell are separated by a vacuum gap with a size of 10 nm, the system can generate a maximum power density of 9.58 W/cm^2 or a maximum conversion efficiency of 9.76%. The maximum conversion efficiency is equivalent to a thermoelectric generator with a ZT of 0.86, calculated based on the formula provided in ref 19. Such high power density and conversion efficiency make this system particularly attractive for solid-state-based waste-heat recovery.

In the presence of a nonzero external bias, photons emitted from a semiconductor can have a nonzero chemical potential.[20] For a semiconductor maintained at temperature T, a positive bias V separates the quasi-Fermi levels of the electrons and holes by qV, where q is the elementary charge.[21,22] A photon gas in equilibrium with such an electron−hole system through interband transitions, i.e., with photon energy above the band gap, follows the modified Bose−Einstein distribution given by:

$$\Theta(\omega, T, V) = \frac{\hbar\omega}{\exp\left(\frac{\hbar\omega - qV}{k_B T}\right) - 1} \tag{1}$$

In eq 1, $\Theta(\omega,T,V)$ is the modified mean energy of a Planck oscillator at angular frequency ω, k_B is the Boltzmann constant, and $\hbar$ is the reduced Planck constant. The term qV is the chemical potential of photons.

Unlike traditional thermophotovoltaic systems that use passive thermal emitters, a thermophotonic system uses an active emitter made of an electrically driven LED with a positive bias V. eq 1 indicates that such an LED can generate a luminescence with an intensity that is much higher than the thermal emission from a passive thermal emitter at the same temperature. Although such a high luminescence intensity comes at the cost of using part of electric power produced by the photovoltaic cell to drive the LED, the power of the electroluminescence can be higher than the consumed electric power because the LED also extracts thermal energy and use it to produce photons. The power enhancement in a thermophotonic system is thus closely related to the effect of electroluminescent cooling in a LED.[15−17,21,23−25]

In our proposed thermophotonic system, the electric power that the system generates, P, is the difference of the power produced by the PV cell and the power pumped into the LED:

$$P = V_{PV}I_{PV} - V_{LED}I_{LED} \tag{2}$$

where V_{PV} and I_{PV} are the voltage and current density for the PV cell and V_{LED} and I_{LED} are the voltage and current density for the LED.

The current densities in eq 2 are related to the above-band-gap photon flux. We calculate the above-band-gap photon flux F from the LED to the cell using the standard formalism of fluctuational electrodynamics.[26−28] For the PV cell, the received photon flux F_{PV} results from the net radiation exchange between the PV cell and the LED, the PV cell and the mirror on the LED side, and the PV cell and the mirror on the PV-cell side:

$$F_{\text{PV}} = \int_{\omega_{\text{c,PV}}}^{\infty} \left[\frac{\Theta_{\text{LED}} - \Theta_{\text{PV}}}{\hbar\omega} \Phi_{\text{LED,PV}} + \frac{\Theta_{\text{m}_{\text{LED}}} - \Theta_{\text{PV}}}{\hbar\omega} \Phi_{\text{PV,m}_{\text{LED}}} \right.$$
$$\left. + \frac{\Theta_{\text{m}_{\text{PV}}} - \Theta_{\text{PV}}}{\hbar\omega} \Phi_{\text{PV,m}_{\text{PV}}} \right] d\omega \tag{3}$$

Similarly, for the LED, the emitted above-band-gap photon flux F_{LED} is received by the PV cell and the mirror on the back of the PV cell as well as the mirror on the back of the LED as follows:

$$F_{\text{LED}} = \int_{\omega_{\text{c,LED}}}^{\infty} \left[\frac{\Theta_{\text{LED}} - \Theta_{\text{PV}}}{\hbar\omega} \Phi_{\text{LED,PV}} + \frac{\Theta_{\text{LED}} - \Theta_{\text{m}_{\text{PV}}}}{\hbar\omega} \Phi_{\text{LED,m}_{\text{PV}}} \right.$$
$$\left. + \frac{\Theta_{\text{LED}} - \Theta_{\text{m}_{\text{LED}}}}{\hbar\omega} \Phi_{\text{LED,m}_{\text{LED}}} \right] d\omega \tag{4}$$

In the above equations, $\Theta_{\alpha} \equiv \Theta(\omega, T_{\alpha}, V_{\alpha})$ as defined in eq 1, subscripts m_{PV} and m_{LED} represent the mirrors on the PV cell and LED side, respectively. ω_{c} is the angular frequency corresponding to the band gap. Φ is defined as:

$$\Phi(\omega) = \frac{1}{4\pi^2} \int_0^{\infty} \xi(\omega, \beta) \beta \, d\beta \tag{5}$$

In eq 5, β is the magnitude of the in-plane wave vector. $\xi(\omega, \beta)$ is the energy transmission coefficient. We use dyadic Green's functions[26] together with the scattering matrix method[29] to calculate the energy transmission coefficients between various components of the system.[28] This formalism applies in the presence of parasitic absorption, e.g., the loss at the mirrors. We model the above-band-gap optical properties of $\text{Al}_x\text{Ga}_{1-x}\text{As}$ based on ref 30. The bias changes the electron and hole population near the band edges and therefore influences the interband transition processes in the semiconductor. Because the above-band-gap absorption is almost entirely due to the interband transitions, the imaginary part of the dielectric function in the frequency range above the band gap is dependent upon the bias. We take into account such bias dependency of the above-band-gap optical properties using the formula as discussed in ref 21. The visible and infrared properties of Ag are from refs 31 and 32, respectively. In the temperature range of 500−700 K, the change of the reflectivity of Ag is roughly 1%.[33] Therefore, we assume the properties of Ag to be temperature-independent.

Eq 5 contains the contributions from both the propagating-wave ($\beta < k_0$) and the evanescent-wave ($\beta > k_0$) channels. Here, k_0 is the magnitude of the wave vector in vacuum. In the far field, only the propagating-wave channels contribute to the power transfer, but in the near-field regime, the evanescent-wave channels contribute dominantly. The overall radiation transfer is thus significantly enhanced in the near-field regime.

With all of the relevant photon fluxes, we calculate the current densities in the PV cell and LED by:

$$I_{\text{PV}} = q[F_{\text{PV}} - R_{\text{PV}}(V_{\text{PV}})] \tag{6}$$

$$I_{\text{LED}} = q[F_{\text{LED}} + R_{\text{LED}}(V_{\text{LED}})] \tag{7}$$

In eqs 6 and 7, R is the net rate of the non-radiative recombination, which can be modeled by:[21]

$$R(V) = (C_n n + C_p P)(np - n_i^2)t + \frac{1}{\tau} \frac{np - n_i^2}{n + p + 2n_i} t \tag{8}$$

In eq 8, n and p are the electron and hole concentrations, respectively, and they are voltage-dependent. C_p and C_n are the

Auger recombination coefficients for holes and electrons, respectively, n_i is the intrinsic carrier concentration, and τ is the bulk Shockley-Read-Hall lifetime. The non-radiative recombination rate is a volumetric effect. Thus, the number of non-radiative recombination events per unit area of the device is proportional to the thickness of the device, as shown in eq 8. We assume the LED and PV cell are n-doped with a doping level of 5×10^{17} cm^{-3} and $\tau = 16.7$ μs based on what have been demonstrated in experiments.[18,34] We also take into account the temperature dependence of C and n_i. We model the temperature dependence of the Auger recombination coefficients using $C = C_0 \exp(-E_a/k_B T)$,[35] where E_a is the activation energy of the Auger processes. We use $E_a = 20$ meV because the Auger recombination is dominated by phonon-assisted processes for the band-gap range considered in this work.[36] We then determine C_0 for compounds with different x based on the data at 300 K.[37] The intrinsic carrier concentration is obtained by $n_i = (N_c N_v)^{1/2} \exp[-E_g/(2k_B T)]$, where E_g is the band gap of the $\text{Al}_x\text{Ga}_{1-x}\text{As}$ at temperature T. N_c and N_v are the effective density of states in the conduction and valence bands, respectively, and their temperature dependence is based on the model for GaAs.[38]

To calculate the radiative heat transfer rate (denoted by E below) between the PV cell and the LED, we integrate the spectral heat flux over the entire frequency range:

$$E = \int_0^{\infty} \left[\begin{array}{l} (\Theta_{\text{LED}} - \Theta_{\text{PV}})\Phi_{\text{LED,PV}} + (\Theta_{\text{LED}} - \Theta_{\text{m}_{\text{PV}}})\Phi_{\text{LED,m}_{\text{PV}}} + \\ (\Theta_{\text{m}_{\text{LED}}} - \Theta_{\text{PV}})\Phi_{\text{PV,m}_{\text{LED}}} + (\Theta_{\text{m}_{\text{LED}}} - \Theta_{\text{m}_{\text{PV}}})\Phi_{\text{m}_{\text{PV}},\text{m}_{\text{LED}}} \end{array} \right]$$
$$d\omega \tag{9}$$

Based on energy conservation, the heat flux extracted from the heat source to the LED is $E - V_{\text{LED}}I_{\text{LED}}$. Thus, the efficiency of the system is:

$$\eta = \frac{P}{E - V_{\text{LED}}I_{\text{LED}}} \times 100\% \tag{10}$$

We use eqs 2 and 10 to find the maximum power density P and efficiency η with respect to V_{PV} and V_{LED}. In general, maximum P and maximum η are achieved at different voltages.

We now discuss the case shown in Figure 1b in detail. In Figure 1b, we show the performance of our system as a function of the voltage on the LED V_{LED}. For each fixed V_{LED}, the curves show the optimized efficiency or power density as we vary the output voltage V_{PV} from the PV cell. In practice, the output voltage of the PV cell can be controlled by choosing the appropriate external load on the PV cell.

In the far-field case in which $d = 1$ μm, when V_{LED} is zero, the LED is a passive thermal emitter and the system operates as a traditional thermophotovoltaic system. In this case, the thermal radiation from the LED that is above the band gap of the PV cell (1.64 eV) is 0.06 nW/cm^2. Thus, the output power density is negligibly small. When the LED is biased, the output power density P can be significantly improved to 270 nW/cm^2 at $V_{\text{LED}} = 0.63$ V, which is about 5 orders of magnitude larger compared to the scenario in which the LED is not biased.

To further enhance the power, we consider the near-field case in which we decrease d to 10 nm, close to the gap spacings that have been demonstrated in recent experiments.[39,40] In doing so, at a higher bias voltage $V_{\text{LED}} = 1.43$ V, the maximum power density P increases to 9.58 W/cm^2, as shown on the solid blue curve. At this maximum power point, the voltage of the PV cell is $V_{\text{PV}} = 1.52$ V. At the maximum power point, the corresponding
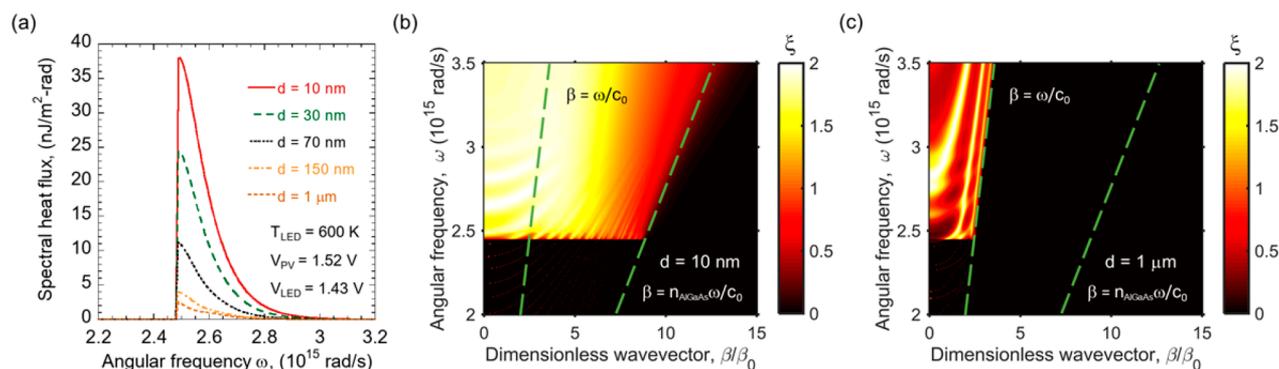
Figure 2. (a) Above-band-gap spectral heat flux between the LED and the PV cell ($Al_{.155}Ga_{.845}As$) at different gap spacings from the near field to the far field. The parameters are T_{LED} = 600 K, V_{PV} = 1.52 V, V_{LED} = 1.43 V, $t_{PV} = t_{LED}$ = 900 nm, and Ag mirrors are used. (b) Transmission coefficient between the hot and cold sides as a function of ω and β for the system when d = 10 nm. The dashed lines are the light lines of vacuum and an AlGaAs compound with a refractive index n_{AlGaAs} = 3.6. Wave vector β is normalized by $\beta_0 = \omega_0/c_0$ with $\omega_0 = 10^{15}$ rad/s and c_0 being the speed of light in a vacuum. (c) Transmission coefficient when d = 1 μm.

efficiency η is 8.47%. The efficiency of the system, η, which is obtained for a fixed voltage of the LED V_{LED} by maximizing the efficiency with respect to the voltage on the PV cell V_{PV}, also follows a similar trend as shown in the solid red curve. The maximum efficiency η, 9.76%, is reached at a lower voltage when V_{LED} = 1.41 V. For comparison, we also show the ideal case assuming zero non-radiative recombination rates and perfect back mirrors. In this case, the system could yield a power density of 97 W/cm², indicating that further improvements are possible.

In all cases considered in Figure 1b, the net power first increases and then decreases when V_{LED} becomes higher. The intensity of the electroluminescence from the LED increases as the voltage on the LED becomes higher, which favors the power generation. However, in general, a higher voltage on the LED would also require a higher-output-voltage V_{PV} for the PV cell. This may be better understood in the case with perfectly reflective mirrors. Based on eqs 6 and 7, the current density I_{LED} in the LED is greater than the current density I_{PV} in the PV cell because of the presence of non-radiative recombination in both the LED and the PV cell. Therefore, the voltage of the PV cell V_{PV} has to be greater than the voltage on the LED V_{LED} to ensure a net power generation based on eq 2. This is also true for the proposed structure that uses highly reflective Ag mirrors. As the voltages become higher, the carrier densities and the non-radiative recombination rate, especially the Auger term, also increase based on eq 8, making the LED and PV cell less efficient and thus reducing the net power output. The two effects thus yield an optimized LED voltage that gives the maximum power P, as shown in Figure 1b. By reducing the non-radiative recombination rates R or by enhancing the net radiative exchange rate F, the optimal operation point of the LED can have higher voltage V_{LED} and, hence, a higher operating power density and higher efficiency.

In the proposed thermophotonic system, we take advantage of the photon tunneling effect in the near-field to significantly increase the net radiative exchange rate F. To better illustrate this effect, we show the above-band-gap spectral heat flux in Figure 2a. We use the same configurations corresponding to the maximum power point of the near-field case in Figure 1b and only decrease the gap spacing gradually from 1 μm to 10 nm. As the gap becomes smaller, the spectral heat flux increases significantly. The high heat flux at small gaps comes from efficient photon tunneling between the PV cell and the LED. Figure 2b shows the energy transmission coefficient ($\xi(\omega,\beta)$ in

eq 5) between the cold and hold sides of the structure as a function of ω and β at d = 10 nm. In the spectral range in Figure 2b, the refractive index of the LED and the PV are both approximately equal to 3.6, and the corresponding light line is shown in Figure 2b, together with the light line of vacuum. We observe significant energy transmission in the $\omega-\beta$ regions between the two light lines, indicating substantial contributions of evanescent tunneling to the heat transfer. The frequency and wave vector in which such high transmission occurs correspond to the waveguide modes of the LED and PV cell structure.[39,41] In contrast, when d = 1 μm, the system is in the far-field regime, and significant energy transmission occurs only in the $\omega-\beta$ regions above the light line of vacuum (Figure 2c). The significant enhancement of the net radiative transfer rate in the near-field regime is therefore directly related to the evanescent tunneling as facilitated by the waveguide modes in the LED and the PV cell.

In addition to the preference to operate in the near-field regime, we highlight a few other design considerations below. In this system, it is critical to use a good mirror on the backsides of the LED and the PV cell. A poor mirror with low reflectivity would absorb the useful photons and degrade the power density and the efficiency of the system. In reality, a lot of factors, such as temperatures and fabrication techniques, could affect the reflectivity of the mirror. Here, rather than assuming a particular physical mechanism that affects the mirror properties, we focus on illustrating the direct effect of the quality of the mirror on the device performance. To do this, we consider the same near-field case as shown in Figure 1b but with the Ag mirror replaced by a mirror made of a hypothetical material. In this way, we can vary the mirror reflectivity continuously. The hypothetical material has the same real part of dielectric function as the Ag mirror, but the imaginary part is varied by multiplying the original imaginary part of Ag by a factor of 0 to 5 so that we can adjust the quality of the mirror in our simulation. Because the real part of the dielectric function is many times larger than its imaginary part, and moreover, the calculation is only over a narrow range of frequencies, the corresponding change of the real part required by the Kramers−Krönig relations would be minimal and has therefore been omitted. To parametrize the quality of the mirror, we first calculate the frequency-dependent reflectivity assuming the mirrors are optically thick and light is incident from a medium on top of the mirror. The medium has a refractive index of 3.6. We then average the frequency-dependent reflectivity in

the normal direction in the above-band-gap frequency range from 2.49×10^{15} to 3×10^{15} rad/s, i.e., a wavelength range of 628 to 756 nm, to obtain the spectral-averaged reflectivity. For each mirror, we optimize either the power density P or the efficiency η by varying both V_{PV} and V_{LED}. In Figure 3a, we show the
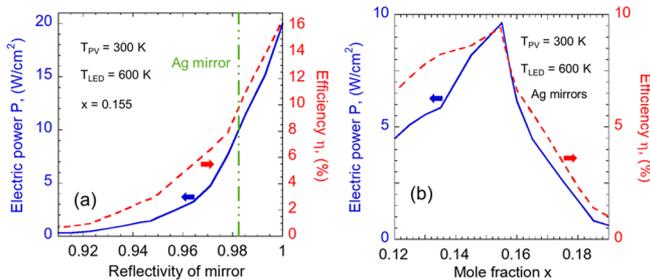

Figure 3. (a) Maximum electric power P and maximum efficiency η as a function of the reflectivity of the mirrors for the LED and the PV cell ($Al_{.155}Ga_{.845}As$). The parameters are fixed at $d = 10$ nm, $T_{LED} = 600$ K, and $t_{PV} = t_{LED} = 900$ nm. The case for Ag mirrors is shown using the vertical green line. (b) Maximum electric power P and maximum efficiency η as a function of the mole fraction of Al in the PV cell using Ag mirrors. The other parameters are the same as the case in panel a.

maximum power density P and the maximum efficiency η thus obtained as a function of the spectral-averaged reflectivity. We see that the mirror reflectivity has a very large impact on the device performance. The structure considered in Figure 1a, which has a mirror reflectivity of 98.2% as represented by the green dashed line in Figure 3a, has a maximum power density of 9.58 W/cm^2 or a maximum efficiency of 9.76%. In contrast, reducing the mirror reflectivity to 90% drastically degenerate the maximum power density and the maximum efficiency to 0.31 W/cm^2 and 0.68%, respectively.

Another important factor that can considerably affect the performance is the alignment of the band gaps of the LED and the PV cell. The band gap of $Al_xGa_{1-x}As$ compounds at temperature T is given by[42,43]

$$E_g(x, T) = E_{g0} - \frac{\alpha T^2}{T + \beta} + 1.36x + 0.22x^2 \tag{11}$$

where $E_{g0} = 1.519$ eV, $\alpha = 5.41 \times 10^{-4}$ eV/K, and $\beta = 204$ K. Because the LED in the system is operating at a temperature higher than the room temperature, using the same material for the LED and the PV cell would result in different band gaps. If such a band gap misalignment is present, useful photons in the frequency range between the band gaps can easily leak out to the mirrors and wasted because the LED and PV cell become essentially transparent below their band gaps. To demonstrate the impact of band-gap misalignment, we consider the near-field case as shown in Figure 1a. we change the mole fraction x of the PV cell and optimize the maximum power density P and maximum efficiency η with respect to the voltages on the LED and PV cell for each mole fraction x. The results are shown in Figure 3b. We see that when $x = 0.155$, which is the value used throughout the paper, the band gaps of the PV cell and the LED are aligned, and the maximum power and maximum efficiency are both maximized to 9.58 W/cm^2 and 9.76%, respectively. In contrast, when $x = 0.19$, the PV cell has a band gap of 1.69 eV that is higher by 0.05 eV compared to the band gap of the LED (1.64 eV). This band-gap mismatch decreases the maximum power density and efficiency down to 0.63 W/cm^2 and 1.03%, respectively. Similarly, the performance of the system also

quickly degrades with decreasing x for $x < 0.155$. Therefore, band-gap matching between the LED and the PV is critical for the high performance of the system.

In contrast to thermophotovoltaic systems, whose power density and efficiency generally become higher at higher temperatures on the hot side, the performance of the thermophotonic system, if a fixed band-gap material was used, would degrade as the temperature of the LED becomes higher than the designed optimal temperature because the band gap of the semiconductor is temperature-dependent, and hence, deviating from the desired temperature will leads to band gap misalignment between the LED and the PV cell. For example, for the structure and materials in Figure 1b, which were optimized for the LED temperature of 600 K, if we increase the LED temperature to 700 K, the maximum power density and efficiency would decrease to 3.69 W/cm^2 and 4.56%, respectively. Alternatively, if we decrease the LED temperature of 500 K, the maximum power density and efficiency decreased even more to 0.225 W/cm^2 and 0.7%, respectively. These results again illustrate that ensuring band gap alignment is crucial to achieving high performance in these systems.

To achieve high performance in this system, in addition to considerations of the mirror reflectivity and the band-gap alignment, it is also essential to seek to reduce the impact of non-radiative recombination in the LED and PV cell. A thicker cell or LED may enable more radiation exchange and result in higher power densities. However, based on eq 8, the non-radiative recombination rate R scales proportionally to the thickness. Therefore, there exists an optimum thickness for the LED and the cell. To demonstrate this effect, we use the same system as shown in Figure 1a for the near-field case, but we vary the thicknesses of the LED and the PV cell. Because the optical properties of the LED and the PV cell are similar in the above-band-gap frequency range, we set the thicknesses $t_{PV} = t_{LED} = t$. For each value of t, we then maximize either the power density or the efficiency by varying the voltages of the cell and the LED. The results are plotted in Figure 4a,b.

For the ideal case with perfect mirrors and zero non-radiative recombination rate R, we see that power density P and efficiency η increase monotonically with the thickness of the LEDs and PV cells, and saturate to 97 W/cm^2 and 24%, respectively, for thicknesses greater than 2 μm. With the more-realistic Ag mirror
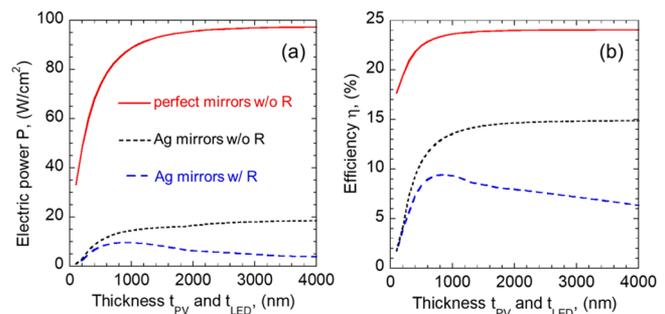

Figure 4. (a) Maximum electric power P and (b) efficiency η as a function of the thickness of the LED and PV cell ($Al_{.155}Ga_{.845}As$). t_{PV} and t_{LED} are set to be equal in the calculation. The temperatures are $T_{PV} = 300$ K and $T_{LED} = 600$ K. The solid line is the ideal case in which the non-radiative recombination rate R (includes both Auger and SRH processes) is 0 for the LED and PV cell and the mirror is perfect. The short-dashed line is the case with Ag mirror but an R of 0 for the LED and PV cell. The long-dashed line is for the case when both non-idealities are considered.

but again assuming that $R = 0$, at a given thickness, both the power density and the efficiency drop due to the mirror loss. The power density and efficiency still saturate at the large thickness, but the saturated values are lower than the ideal case because the LED and PV cell are still losing photons to their backside mirrors. Although an Ag mirror with 98.2% reflectivity is used, we observe a significant degradation of the saturated power density from 97 to 18.4 W/cm^2, indicating that a high-reflectivity mirror is critical to the high performance of the system. One may mitigate the photon loss through the mirrors by using a thicker confinement layer. The confinement layer reduces the near-field electromagnetic coupling between the back mirror and the semiconductors, which is a substantial parasitic loss mechanism of the system when the imperfect mirror and active region are separated by less than a few hundred nanometers. This loss mechanism persists as long as the chemical potentials of photons in the LED and the PV cell are nonzero. It becomes the dominant loss mechanism when the gap spacing between the LED and the PV becomes larger. Therefore, using a thicker confinement layer is critical for high performance especially when the gap spacing is large. Once the non-radiative recombination is added, the power density P and efficiency η both maximize at $t_{LED} = t_{PV} = 900$ nm with values of 9.58 W/cm^2 and 9.76%, respectively. Further increasing the thickness beyond such an optimal point reduces both the power density and the efficiency. In general, increasing the non-radiative recombination rate resulting in an optimal structure with thinner cells and LEDs.

We further evaluate the maximum power density and maximum efficiency of the proposed system at different gap distances and temperatures at the hot side, shown in panels a and b of Figure 5, respectively. We include the non-radiative
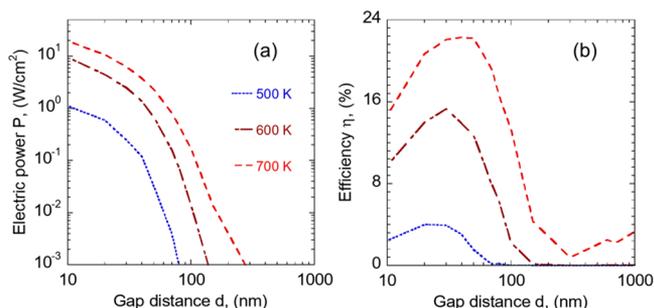

Figure 5. (a) Maximum electric power P and (b) maximum efficiency η as a function of the gap distance and the temperature of the LED.

recombination and assume Ag mirrors. For each temperature and gap distance, we allow the thickness and the voltages of the PV cell and LED to change until the power density or efficiency is optimized. Therefore, each point on the curves can represent a structure with different x, t_{LED} ($= t_{PV}$), V_{PV}, and V_{LED}.

Because the power carried by the above-band-gap photons represents a larger portion of the total emitted power as the temperature increases, the maximum power density P and efficiency η have the same trend, and both increase as the temperature increases. However, P and η do not follow the same trend as the gap distance d changes. As the gap becomes smaller, the photon tunneling becomes stronger and hence power density becomes higher, as indicated in Figure 5a. However, for all three temperatures considered here, there is an optimal gap distance that maximizes the efficiency, as indicated in Figure 5b. Reducing the gap distance below such an optimal gap distance

reduces the efficiency. At small gap distances, the surface phonon polaritons[11,44] contribute significantly to the below-band-gap heat transfer because both the LED and the PV cell are made of polar dielectric materials,[45] which reduces the efficiency.[11,46]

With the thermophotonic system, one need not choose a narrow-band semiconductor, even when recovering low-grade waste heat. In our design, the AlGaAs system has a gap of about 1.6 eV, which is much larger than the energy scale that corresponds to a temperature of 600 K. We choose the AlGaAs ternary system mainly because of its relatively low non-radiative recombination rate. In the AlGaAs system, higher-band-gap compounds experience relatively less non-radiative Auger recombination at a given temperature and carrier density. We chose a compound with a band gap of 1.64 eV for the LED because AlGaAs compound with larger band gap becomes indirect with reduced radiative efficiency. Other semiconductors may be used for such a system as well. For example, one may consider using nonpolar semiconductors such as Si and Ge on the PV cell side to eliminate the phonon-polariton effects.[46] One may also consider using high-temperature-stable semiconductors such as GaN to recover waste heat at a higher temperature.

In conclusion, we propose a near-field thermophotonic system based on $Al_xGa_{1-x}As$ semiconductors for high-performance, low-grade waste-heat recovery. The system consists of a light-emitting diode on the hot side and a photovoltaic cell on the cold side, with some of the power generated by the cell used to positively bias the light emitting diode. By operating in the near-field regime, this system can have efficiency and power density significantly exceeding the performance of existing solid-state approaches for low-grade heat. Our findings demonstrate the great potential of using photonic approaches for waste-heat-recovery applications.

■ AUTHOR INFORMATION

Corresponding Author
*E-mail: shanhui@stanford.edu.
ORCID ⦿
Bo Zhao: 0000-0002-3648-6183
Notes
The authors declare no competing financial interest.

■ REFERENCES

(1) ICF International. *Waste Heat to Power Market Assessment for Oak Ridge National Laboratory*; ICF International: Fairfax, VA, 2015.
(2) BCS, Inc. *Waste Heat Recovery: Technology and Opportunities in U.S. Industry for the U.S. Department of Energy Industrial Technologies Program*; BCS: Hinsdale, IL, 2008.
(3) Liu, W.; Jie, Q.; Kim, H. S.; Ren, Z. *Acta Mater.* **2015**, *87*, 357−376.
(4) Alam, H.; Ramakrishna, S. *Nano Energy* **2013**, *2*, 190−212.
(5) He, R.; Kraemer, D.; Mao, J.; Zeng, L.; Jie, Q.; Lan, Y.; Li, C.; Shuai, J.; Kim, H. S.; Liu, Y.; Broido, D.; Chu, C.-W.; Chen, G.; Ren, Z. *Proc. Natl. Acad. Sci. U. S. A.* **2016**, *113*, 13576−13581.

(6) Wedlock, B. D. *Proc. IEEE* **1963**, *51*, 694−698.

(7) Chan, W. R.; Bermel, P.; Pilawa-Podgurski, R. C. N.; Marton, C. H.; Jensen, K. F.; Senkevich, J. J.; Joannopoulos, J. D.; Soljačić, M.; Celanovic, I. *Proc. Natl. Acad. Sci. U. S. A.* **2013**, *110*, 5309−5314.

(8) Bierman, D. M.; Lenert, A.; Chan, W. R.; Bhatia, B.; Celanović, I.; Soljačić, M.; Wang, E. N. *Nat. Energy* **2016**, *1*, 16068.

(9) Park, K.; Basu, S.; King, W. P.; Zhang, Z. M. *J. Quant. Spectrosc. Radiat. Transfer* **2008**, *109*, 305−316.

(10) Ilic, O.; Jablan, M.; Joannopoulos, J. D.; Celanovic, I.; Soljačić, M. *Opt. Express* **2012**, *20*, A366−A384.

(11) Zhao, B.; Chen, K.; Buddhiraju, S.; Bhatt, G.; Lipson, M.; Fan, S. *Nano Energy* **2017**, *41*, 344−350.

(12) St-Gelais, R.; Bhatt, G. R.; Zhu, L.; Fan, S.; Lipson, M. *ACS Nano* **2017**, *11*, 3001−3009.

(13) Liu, X. L.; Wang, L. P.; Zhang, Z. M. *Nanoscale Microscale Thermophys. Eng.* **2015**, *19*, 98−126.

(14) Harder, N. P.; Green, M. A. *Semicond. Sci. Technol.* **2003**, *18*, S270.

(15) Oksanen, J.; Tulkki, J. *J. Appl. Phys.* **2010**, *107*, 093106.

(16) Chen, K.; Xiao, T. P.; Santhanam, P.; Yablonovitch, E.; Fan, S. *J. Appl. Phys.* **2017**, *122*, 143104.

(17) Liu, X.; Zhang, Z. M. *Nano Energy* **2016**, *26*, 353−359.

(18) Steranka, F. M. *Semicond. Semimetals* **1997**, *48*, 65−96.

(19) Snyder, J. G.; Ursell, T. S. *Phys. Rev. Lett.* **2003**, *91*, 148301.

(20) Wurfel, P. *J. Phys. C: Solid State Phys.* **1982**, *15*, 3967.

(21) Chen, K.; Santhanam, P.; Sandhu, S.; Zhu, L.; Fan, S. *Phys. Rev. B: Condens. Matter Mater. Phys.* **2015**, *91*, 134301.

(22) Lin, C.; Wang, B.; Teo, K. H.; Zhang, Z. *J. Appl. Phys.* **2017**, *122*, 243103.

(23) Tauc, J. *Czech. J. Phys.* **1957**, *7*, 275−276.

(24) Weinstein, M. A. *J. Opt. Soc. Am.* **1960**, *50*, 597−602.

(25) Santhanam, P.; Gray, D. J.; Ram, R. J. *Phys. Rev. Lett.* **2012**, *108*, 097403.

(26) Polder, D.; Van Hove, M. *Phys. Rev. B* **1971**, *4*, 3303−3314.

(27) Zhang, Z. M. *Nano/Microscale Heat Transfer*; McGraw-Hill: New York, 2007.

(28) Chen, K.; Zhao, B.; Fan, S. *Comput. Phys. Commun.* **2018**, *231*, 163−172.

(29) Whittaker, D. M.; Culshaw, I. S. *Phys. Rev. B: Condens. Matter Mater. Phys.* **1999**, *60*, 2610−2618.

(30) Adachi, S. *Phys. Rev. B: Condens. Matter Mater. Phys.* **1988**, *38*, 12345−12352.

(31) Johnson, P. B.; Christy, R. W. *Phys. Rev. B* **1972**, *6*, 4370−4379.

(32) Zhao, B.; Zhang, Z. M. *J. Quant. Spectrosc. Radiat. Transfer* **2014**, *135*, 81−89.

(33) Ujihara, K. *J. Appl. Phys.* **1972**, *43*, 2376−2383.

(34) Imangholi, B.; Hasselbeck, M. P.; Sheik-Bahae, M.; Epstein, R. I.; Kurtz, S. *Appl. Phys. Lett.* **2005**, *86*, 081104.

(35) Seki, S.; Lui, W. W.; Yokoyama, K. *Appl. Phys. Lett.* **1995**, *66*, 3093−3095.

(36) Steiauf, D.; Kioupakis, E.; Van de Walle, C. G. *ACS Photonics* **2014**, *1*, 643−646.

(37) Pavesi, L.; Guzzi, M. *J. Appl. Phys.* **1994**, *75*, 4779−4842.

(38) I. P.-T. Institute. *NSM archive - physical properties of semiconductors*; The Ioffe Physical-Technical Institute of the Russian Academy of Sciences, 1998, http://www.ioffe.ru/SVA/NSM/Semicond/.

(39) Kim, K.; Song, B.; Fernández-Hurtado, V.; Lee, W.; Jeong, W.; Cui, L.; Thompson, D.; Feist, J.; Reid, M. T. H.; García-Vidal, F. J.; Cuevas, J. C.; Meyhofer, E.; Reddy, P. *Nature* **2015**, *528*, 387−391.

(40) Fiorino, A.; Zhu, L.; Thompson, D.; Mittapally, R.; Reddy, P.; Meyhofer, E. *Nat. Nanotechnol.* **2018**, 1−6.

(41) Tong, J. K.; Hsu, W.-C.; Huang, Y.; Boriskina, S. V.; Chen, G. *Sci. Rep.* **2015**, *5*, 10661.

(42) Aspnes, D. E. *Phys. Rev. B* **1976**, *14*, 5331−5343.

(43) Gehrsitz, S.; Reinhart, F. K.; Gourgon, C.; Herres, N.; Vonlanthen, A.; Sigg, H. *J. Appl. Phys.* **2000**, *87*, 7825−7837.

(44) Shen, S.; Narayanaswamy, A.; Chen, G. *Nano Lett.* **2009**, *9*, 2909−2913.

(45) Glembocki, O. J.; Takarabe, K. Aluminum Gallium Arsenide ($Al_xGa_{1-x}As$). In *Handbook of Optical Constants of Solids*; Academic Press: Burlington, VT, 1997; pp 513−558.

(46) Chen, K.; Santhanam, P.; Fan, S. *Appl. Phys. Lett.* **2015**, *107*, 091106.

■ NOTE ADDED AFTER ASAP PUBLICATION

This paper was published ASAP on July 20, 2018, with errors in eq 8. The corrected version was reposted on July 23, 2018.